1 # Frequency-specific meso-scale structure of spontaneous oscillatory activity in
2 # the human brain

3 Riccardo Iandolo[1]*, Marianna Semprini[1], Dante Mantini[2,3], Stefano Buccelli[1], Diego Sona[4,5],
4 Laura Avanzino[6,7#], and Michela Chiappalone[1#]

5 *Corresponding Author

6 #Equal Senior Author

7 [1] Rehab Technologies, Istituto Italiano di Tecnologia, 16163 Genova, Italy;

8 [2] Research Center for Motor Control and Neuroplasticity, KU Leuven, 3001 Leuven, Belgium;

9 [3] Brain Imaging and Neural Dynamics Research Group, IRCCS San Camillo Hospital, 30126 Venice, Italy;

10 [4] Pattern Analysis & Computer Vision, Istituto Italiano di Tecnologia, 16152, Genova, Italy;

11 [5] Neuroinformatics Laboratory, Fondazione Bruno Kessler, 38123 Povo (Trento), Italy;

12 [6] Department of Experimental Medicine, Section of Human Physiology, University of Genova, 16132
13 Genova, Italy;

14 [7] Ospedale Policlinico San Martino, IRCCS, 16132 Genova, Italy.

15

16 **<u>Corresponding Author</u>**

17 Dr. Riccardo Iandolo, PhD

18 Rehab Technologies IIT-INAIL Lab

19 Istituto Italiano di Tecnologia

20 Via Morego 30

21 16163 Genova Italy

22 e-mail: riccardo.iandolo@iit.it

23

24

25

1

Abstract

26

27 Recent studies provided novel insights into the meso-scale organization of the brain, highlighting the co-
28 occurrence of different structures: classic assortative (modular), disassortative and core-periphery.
29 However, the spectral properties of the brain meso-scale remain unexplored. To fill this knowledge gap,
30 we investigated how this meso-scale structure is organized across the frequency domain. We analyzed the
31 resting state activity of healthy participants with source-localized high-density electroencephalography
32 signals. Then, we inferred the community structure using weighted stochastic block-modelling to capture
33 the landscape of meso-scale structures across the frequency domain. Despite meso-scale modalities were
34 mixed over the entire spectrum, we found a selective increase of disassortativity in the delta/theta bands,
35 and of core-peripheriness in the low/high gamma bands. We observed, for the first time, that the brain at
36 rest shows frequency-specific meso-scale organizations supporting spatially distributed and local
37 information processing, shedding new light on how the brain coordinates information flow.

38

Introduction

Functional connectivity (FC), i.e. the statistical association among neural signals of separate brain regions (*1*), has received a great deal of attention during the last years (*2*). FC has been widely recognized as a tool to investigate spatio-temporal properties of brain networks. These networks have been characterized at different levels of topological organization (*3*), ranging from local (single brain area or node) to global (whole-brain network) (*4*), through the intermediate level referred to as meso-scale (*5*). The single unit of the meso-scale architecture is a "community" (or module), which is composed by a set of nodes sharing similar connectivity patterns. Modules are crucial elements of FC network organization since they are essential to identify areas belonging to the same functional domain. Moreover, modules well describe network resilience and flexibility in response to external perturbation (as in the case of occurred cerebral lesions) and also they shape the information flow (*6*). To date, the meso-scale structure of the human brain has been extensively investigated by community detection algorithms prone to detect "assortative" (also defined as "modular") meso-scale structure (*5, 7, 8*), for a review see (*9*). Briefly, in the assortative structure, the within-community densities are greater than the between-community densities. In other words, this structure facilitates information processing of segregated modules while the integration capability between them is reduced (*10*).

Recently, non-assortative community interactions have been also described, such as the "disassortative" and the "core-periphery" (*5*). A disassortative structure is complementary to the assortative one . This is characterized by the connections between communities being greater than within communities, thus suggesting a strong flow of information between different modules. In the core-periphery structure, the nodes of a high-density *core* strongly interact with nodes of other *periphery* communities, which are characterized by poorly connected nodes. This structure thus allows an efficient broadcasting of information between core and peripheries (*10*). Importantly, it has been recently shown that these three classes (i.e. assortative, disassortative and core-periphery) may coexist in the brain, forming the so-called mixed meso-scale structure (*5, 9*). Therefore, it is pivotal to detect the richness and diversity of meso-scale organization, without being constrained by the assortative one (*5, 10*). To this purpose, algorithms have been proposed in the literature (*11*), such as the Weighted Stochastic Block Model (*12*) (WSBM) able to capture the meso-scale diversity. An important feature of WSBM is the exploitation of the stochastic equivalence principle, according to which the network nodes belonging to a given community have the same probability of being connected with all the remaining nodes of the network (*12*). The WSBM can detect other modalities of meso-scale modules interactions, beyond assortativity (*5*). Recent studies investigating human (*5, 10, 13*) and non-human networks (*14, 15*) made use of the WSBM method. In these investigations, human connectomes were derived with magnetic resonance imaging (MRI), using either functional (during both rest (*5*) and task (*10*)) or structural data (*5, 13*). In particular, it was observed that assortative communities dominate resting state FC with the co-existence of other non-assortative communities (*10*). Overall, these results indicated that brain networks are not characterized by a unique community structure.

Motivated by the above findings, we aimed at investigating whether resting state FC meso-scale structures can exhibit a more diverse and richer organization when using non-invasive electrophysiological techniques. Notably, high-density electroencephalography (hdEEG) provides a unique opportunity to capture the richness of neuronal oscillations' spectral content (*16*). HdEEG was recently employed to reconstruct and unravel novel features of human brain activity during resting state in health (*17-19*) and disease (*20-23*). By coupling hdEEG recordings with appropriately built head model conductors and with source reconstruction algorithms, it is possible to achieve neural source reconstruction with relatively good spatial resolution (*24*) (in the order of less than 1 cm). This permitted the estimation of large-scale resting state networks that spatially overlap with those obtained with functional MRI (fMRI) (*18*) and

84 magnetoencephalography (MEG) (*25*). Thus, we posit that describing the time-frequency features of FC
85 meso-scale architecture estimated from source-localized hdEEG recordings will have important
86 implications to highlight novel properties of the human brain at rest (*26-28*).

87 With this aim, we here exploited the peculiar features of hdEEG-based source imaging, to identify modules
88 of spontaneous oscillatory activity. Specifically, we tested whether the meso-scale structure is frequency-
89 dependent. In other terms, we examined if assortative, disassortative and core-periphery modalities are
90 tuned onto a specific frequency or they are equally distributed over the frequency domain. To address these
91 questions, we applied the WSBM to FC adjacency matrices estimated from source-localized hdEEG
92 recordings of healthy participants (*17, 18, 29*). We first selected the best number of communities to perform
93 WSBM community detection with a data-driven approach. Then, we defined the cortical and sub-cortical
94 spatial distribution of modules in both time and frequency domains, respectively, and we finally described
95 the assortative, disassortative and core-periphery community interactions across frequency bands. Thus, we
96 observed that the brain at rest relies on peculiar topological meso-scale organization supporting spatially
97 distributed and local information processing. Our results improve and extend the knowledge of resting state
98 meso-scale organization and the way in which the brain propagates the information, leveraging the
99 frequency-specific variability of the meso-scale structure.

100

Results

102 In this study, we reconstructed neural sources per each participant and we then mapped them onto 384
103 regions of interest (ROIs) of the AICHA atlas (*30*). This procedure defined the nodes for the subsequent
104 meso-scale structure investigation. We then extracted the FC adjacency matrices and applied the WSBM.
105 We investigated the organization of the meso-scale structure across time (i.e. full bandwidth) and
106 frequencies. When presenting the results, we localized the wavelet carrier frequencies (i.e. 2, 4, 8, 16, 32
107 and 64 Hz) to the corresponding EEG spectral bands, as in our previous work (*29*), where the bands are
108 defined as delta (δ, 1-4 Hz), theta (θ, 4-8 Hz), alpha (α, 8-13 Hz), beta (β, 13-30 Hz), and gamma (γ, 30-80
109 Hz).

Identification of meso-scale communities

111 To evaluate the clustering performance, we used the Normalized Variation of Information (NVI), which
112 identify a good clustering performance with values near to zero (*31*). Searching for a good clustering, we
113 made experiments with a variable number of cluster K, ranging from 2 to 16 and we observed (see Figure
114 1) that only with less than 6 clusters the clustering performance was good (0.0079 ± 0.0023, 0.011 ± 0.0036,
115 0.014 ± 0.012, and 0.015 ± 0.0059, mean $\pm$ SD, for K=2,..,5 respectively). We excluded K = 2 from the
116 range of possible solutions because for this value we could only had one community interaction, preventing
117 us from investigating the meso-scale richness. With K = 4 communities, some fits terminated in different
118 local maxima (see light-blue lines in Figure 1a and red crosses in Figure 1b) leading to a higher degree of
119 variability than K = 3 and K = 5. Instead, for K $\geq$ 6, the NVI values increased sharply, suggesting that
120 greater K-values were not worth being considered.
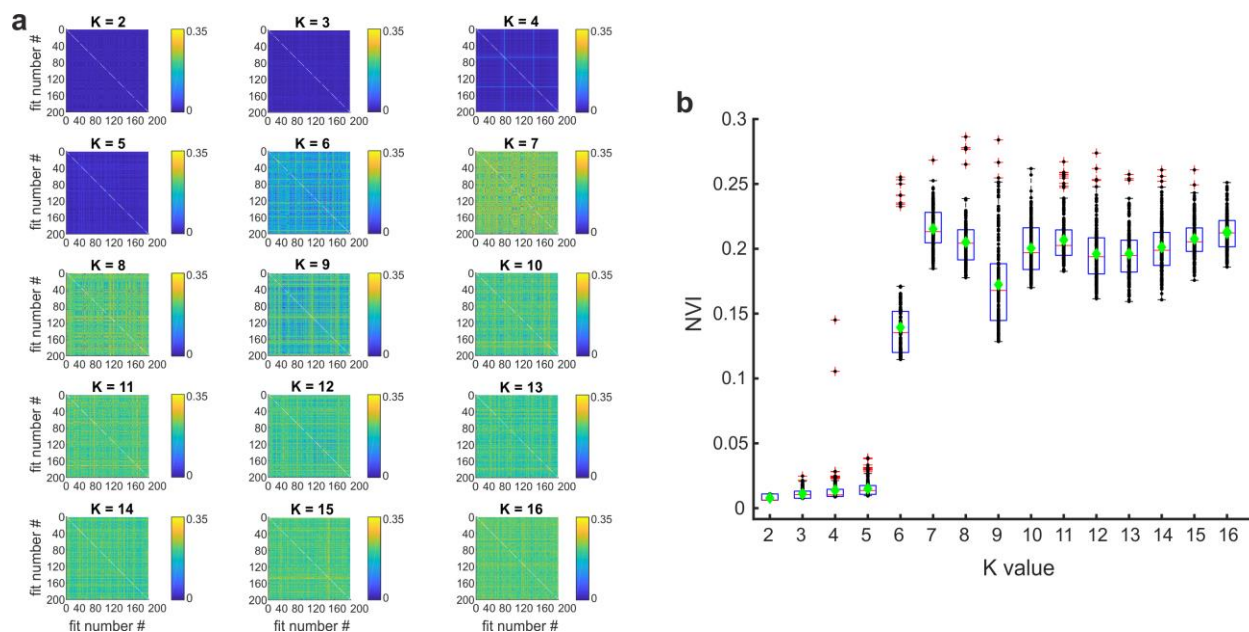
Fig. 1. Parameter selection conducted by means of Normalized Variation of Information (NVI). a Pairwise comparisons of all the 200 fits from K = 2 until K = 16. Dark blue and yellow elements indicate respectively a pair of fits showing a good (low NVI) and weak (high NVI) clustering performance, as indicated by the colorbar. Self-fit comparisons are depicted in white. Note that all the matrices are symmetric. **b** Distributions of the NVI values obtained by averaging the matrices containing the fits' pairwise comparisons depicted in panel a. Boxplots' upper and lower boundary exhibited 25th and 75th percentile, respectively. Data points (black dots) are overlaid over boxplots. Green diamonds and red lines indicates mean and median value of the distributions, respectively. Red crosses indicate outliers.

Despite the fact that the optimization problem was non-convex, the WSBM converged almost always to the same solution for K-values smaller than 6, as shown by the small variability of the NVI (see boxplots in Figure 1B). For those values, the variance of the data was small when compared to the variance for the higher values of $K \geq 6$ (Figure 1b). The reached local maxima were not consistent for higher K values, suggesting that the algorithm struggled to get similar results across trials. Thus, the assessment of the clustering performance suggested to partition the resting state activity with the K-values for which the NVI was closer to zero. Among these values, we selected K = 5 as K_{best} because: i) it offered a good compromise between the granularity of FC network parcellation and reliable clustering performance; ii) it was consistent with similar choices made in recent fMRI literature of WSBM applied to human connectome datasets (*5, 10*). To check whether the clustering performance showed a consistent behavior across K-values, we also calculated other performance parameters: the Adjusted Rand Index (*32*) (ARI) and the Normalized Mutual Information (*31*) (NMI) (see Methods) that both led to the same outcome (Supplementary Figure S1 and Supplementary Figure S2).

Meso-scale connectivity structure in time domain

The original full bandwidth adjacency matrix (ADJ^T, where the superscript T refers to time domain, see Methods and Figure 2, panel a1) was reordered based on the WSBM community assignment (with k_{best} = 5, see Figure 2, panel a2), which was then overlaid onto the T1-weighted template (see Figure 2b) to better appreciate its spatial distribution (see Methods for details about the computation of best community assignment). The first community (purple cluster) showed a medial and lateral spatially distributed pattern.

5
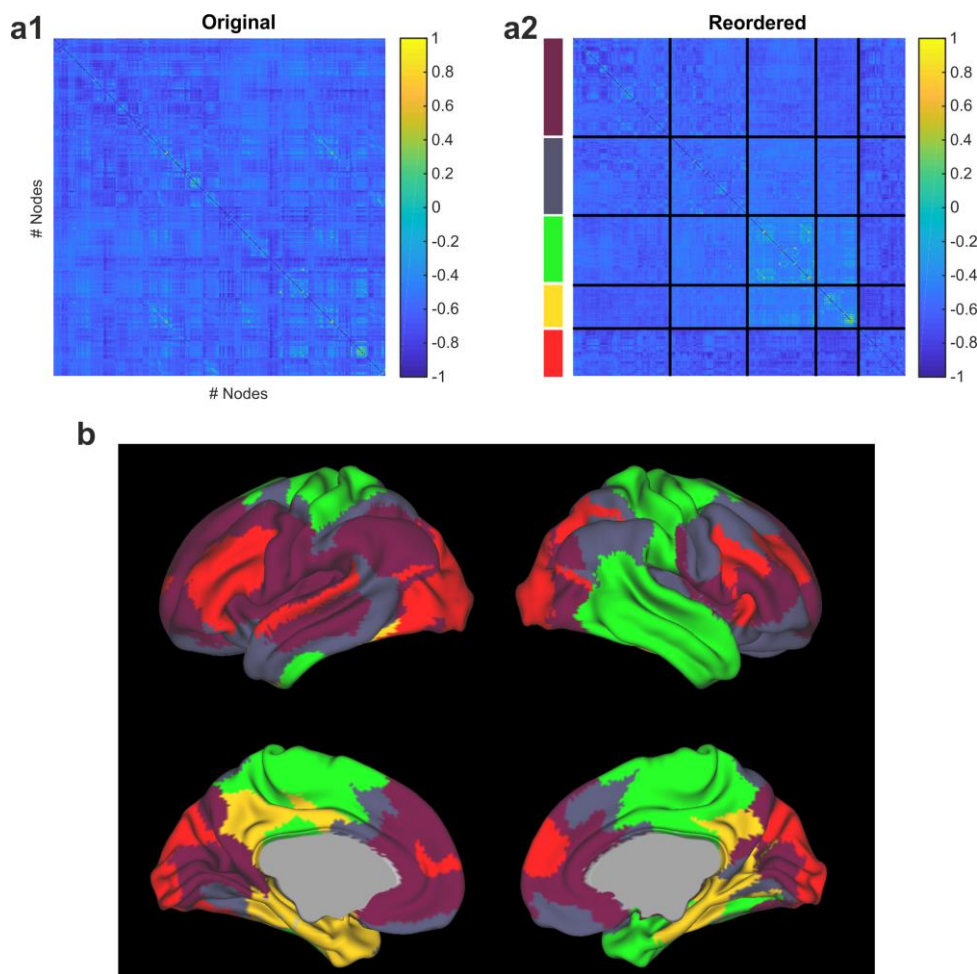
Fig. 2. Community assignment at $K_{best} = 5$ for the group-representative matrix in the time domain. **a1** Adjacency matrix prior to community detection (nodes of the AICHA atlas, $N = 384 \times 384$). First 192 and last 192 nodes indicated left and right hemisphere, respectively. The colorbar represents connection strength mapped onto the interval $[-1, +1]$, see Methods. **a2** Reordered adjacency matrix according to the best community assignment after WSBM estimation. Colored rectangles on the left side of the adjacency matrix represent the 5 resulting clusters. **b** Spatial distribution of the best estimated communities, cluster colors as in a2.

Despite its intrinsic variability, it can be roughly associated with an executive function as it largely covers the left frontal lobe. As the first, also the second community (dark gray cluster) exhibited a complex spatial distribution. In this case, the left areas clustered predominantly in parieto-temporo-occipital (PTO) cortex while the right areas in frontal lobe. On the other hand, the remaining three clusters presented a compact spatial localization (in particular in the medial areas). We assigned them to three separate functional domains: mostly sensorimotor (bilateral motor and sensory cortices encompassing also the right temporal lobe, green cluster), limbic (medial temporal lobe and cingulate gyrus, yellow cluster) and visual (occipital lobe, red cluster). However, the latter approximately spanned other cortical areas, until the frontal and left temporal lobe and this occipital-fronto-temporal gradient resembled the ventral and dorsal streams linked to visual stimuli processing. Then, we investigated the between-community interactions across participants, calculating the percentage of assortative, disassortative and core-periphery motifs in the time domain. We found a significant effect of the meso-scale classes (Kruskal-Wallis test, $p < 0.0001$, see Figure 3a).

6
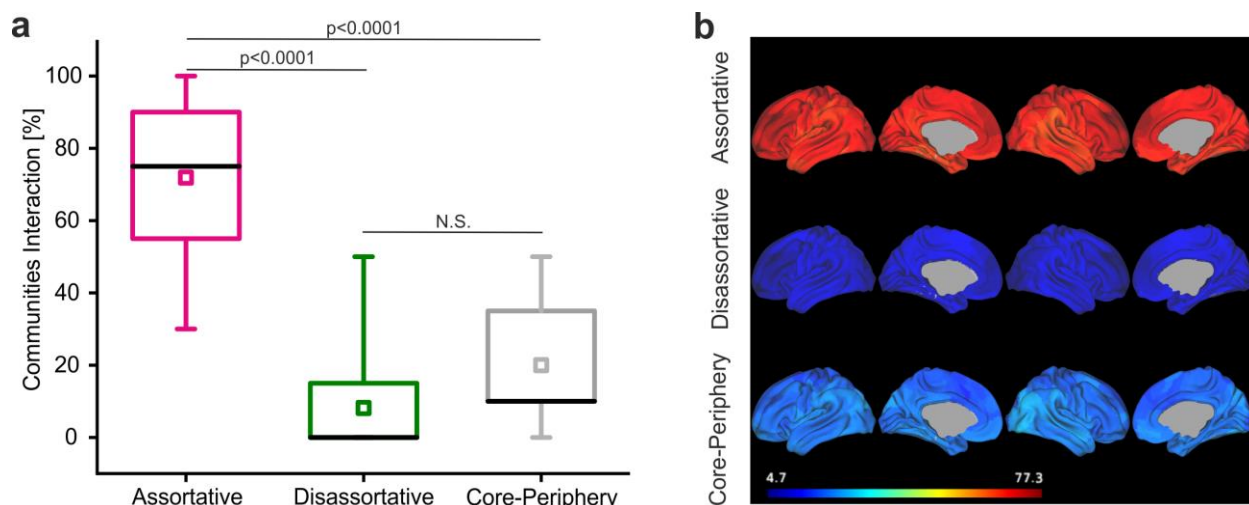
Fig. 3. Organization of the meso-scale structure in the time domain. **a** Boxplots representing distribution of the meso-scale classes across participants. Magenta: assortative; green: disassortative; gray: core-periphery. Boxplots show upper and lower bound of the distributions at 25th and 75th percentile. Whiskers indicate the 1st and 99th percentile. The black horizontal lines represent the median, while the small colored squares indicate the mean of the distributions. N.S. indicates non-statistically significant comparison as revealed by post-hoc comparison of mean ranks. **b** Mean community classes across participants: assortative (top), disassortative (middle) and core-periphery (bottom). The colorbar is kept fixed to the minimum and maximum values across the meso-scale modalities. See Figure S3 in the Supplementary Materials where the same plot is showed with a different colorbar for each meso-scale interaction.

Furthermore, the post-hoc test for multiple comparisons showed a significant increment of the assortative with respect to both disassortative and core-periphery structure (p < 0.0001 in both cases, see Figure 3a). Instead, there was no significant difference between the disassortative and core-periphery class (p = 0.067, see Figure 3a). This can be observed also in Figure 3b (and Figure S3 in Supplementary Materials) where we overlaid the percentages of the three modalities onto the T1-weighted template. As expected, we observed that the meso-scale spatial organization of the source-level time courses reflected the behavior depicted in Figure 3a. In fact, there was a clear whole-brain predominance of the assortative structure (see Figure 3b). Brain regions which showed the greatest assortativity level were located in bilateral medial and lateral prefrontal cortices as well as in the occipital lobe visual areas (yellow and red regions, top row Supplementary Figure S3). These were the areas with low disassortative interaction (blue-light blue regions, middle row Supplementary Figure S3). Conversely, the areas showing higher level of disassortativity are medial areas such as the posterior cingulate cortex together with the sensorimotor and temporal cortex. Furthermore, the areas exhibiting the greatest level of core-periphery structure were focally localized in the PTO cortex (yellow and orange regions, bottom row Supplementary Figure S3).

Frequency analysis of meso-scale connectivity structure

We examined the community assignments across the six carrier frequencies considered ($ADJ^F(f)$, where the superscript F refers to frequency domain and f are the wavelets' carrier frequencies, see Methods). As for the delta band (see Figure 4, panel a1), we obtained an association cluster, almost entirely located in the right hemisphere (corresponding roughly to somatic areas, and association PTO cortex, purple). Another lateralized cluster was obtained in the left hemisphere, putatively associated with executive functions (frontal and temporal lobe, dark gray). Finally, we obtained a "limbic" cluster, related to phylogenetically

7

200 old regions (medial areas in both hemisphere, orbito-fontal cortex, green cluster). The remaining two
201 clusters were spanning several areas (the primary and premotor cortices bilaterally and parietal lobe, yellow
202 and red clusters).

203
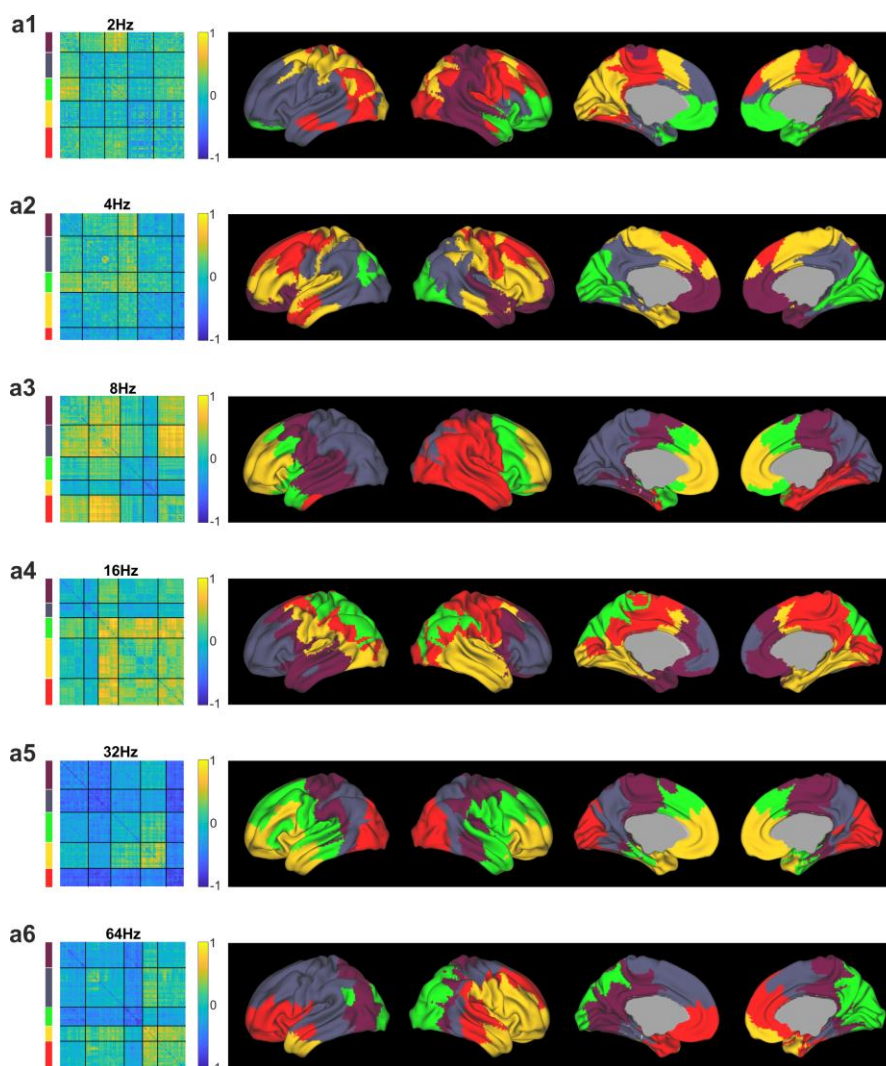
Fig. 4. Organization of the meso-scale structure in the frequency domain. Each row represents the best community
assignments ($K_{best} = 5$) in each of the considered carrier frequency: 2 Hz (**a1**), 4 Hz (**a2**), 8 Hz (**a3**), 16 Hz (**a4**), 32 Hz
(**a5**), 64 Hz (**a6**). Each row contains the re-ordered group-representative adjacency matrix after WSBM estimation
and spatial distribution of partitions across the brain. Colors on left side of each adjacency matrix match with the
colors overlaid on the brain.

209 As for the theta oscillations (see Figure 4, panel a2), the block-modelling partitioning associated brain areas
210 in the medial orbito-frontal cortex (purple), in the parietal lobe and posterior cingulate cortex (PCC)
211 ("sensory association" cluster, dark gray), in the visual areas (primary and higher order visual cortices,
212 green), in the frontal and parietal lobes (a "mixed" cluster, yellow) and in the frontal and temporal cortices
213 (red cluster).

214 As for the alpha rhythm (see Figure 4, panel a3), the generated cluster were approximately the left temporal
215 and frontal lobe (purple), the sensory multimodal regions (primary and secondary visual cortices and the
216 associated dorsal stream, dark gray), the right and left premotor areas (green), the limbic structures (yellow)

8

217 and the right PTO cortex (red). The latter cluster, roughly recalled the association cluster of the lower delta
218 oscillations.

219 As for the beta band (see Figure 4, panel a4), the clusters covered bilateral premotor and prefrontal cortices
220 (purple and dark gray), and mixed areas, with a cluster spanning the dorsal areas in the parietal lobe (green),
221 bilateral temporal lobes (mainly right) and left prefrontal association cortex (yellow), PTO and cingulate
222 cortices (red).

223 As for the low gamma oscillations (see Figure 4, panel a5), the clustering showed two sensory partitions:
224 one that mainly gathered the primary and secondary somatosensory areas in the parietal lobe (purple) and
225 the posterior parietal cortex (dark gray). Other clusters correspond to the executive cluster (motor and
226 prefrontal cortex, green), the limbic cluster (yellow) and the visual cluster (red).

227 Finally, as for the high gamma rhythm (see Figure 4, panel a6), a parietal and cingulate cortex cluster
228 emerged (purple) together with a "sensori-motor" cluster (bilateral sensorimotor cortices, expanding to left
229 temporal lobe, dark gray). A third cluster was located in the occipital lobe (green). Lastly, we found two
230 clusters (yellow and red) predominantly encompassing limbic areas, as well as orbito-frontal and prefrontal
231 cortex.

232 Overall, for brain areas close to the midline, we found more symmetric spatial distribution of clusters than
233 in the laterally located areas. Indeed, when moving towards more lateral regions, the clusters spatial pattern
234 became more complex than the one observed in medial areas. Furthermore, we found that higher rhythms
235 were more likely characterized by functionally distinct clusters than lower frequencies.
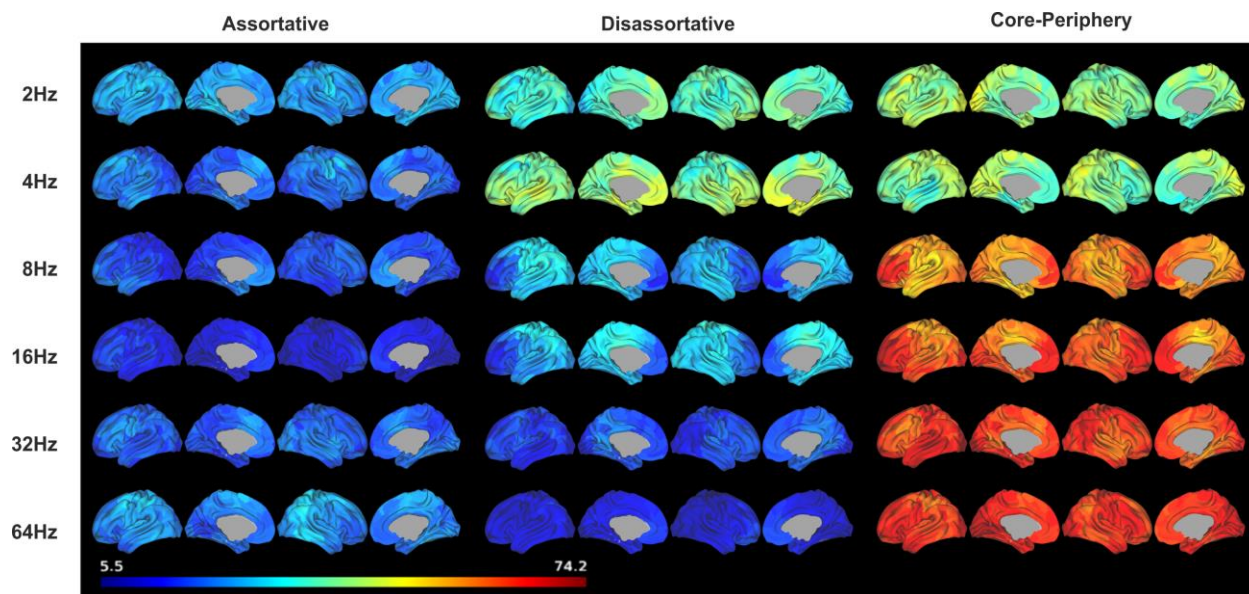
Community structure in the frequency domain is diverse and non-assortative

237 To answer the question whether meso-scale structure is frequency-specific, we investigated possible
238 differences among the six carrier frequencies considering all three community classes (i.e. assortative,
239 disassortative, core-periphery). For the assortative class, we did not find any significant difference across
240 the six bands (p = 0.083), suggesting that the assortative structure is homogeneously distributed across
241 frequency bands (see Figure 5a). Instead, we had a statistically significant effect concerning the
242 disassortative and core-periphery structure (for both, p < 0.0001), as revealed by non-parametric testing.
243 Specifically, modules of spontaneous activity interacted in a more disassortative manner in the delta and
244 low theta bands (2 Hz, 4 Hz) than the beta and gamma bands (32 Hz, 64 Hz), see Figure 5a and
245 Supplementary Table 1. In addition, a further decrease, albeit weakly significant (p = 0.045, see
246 Supplementary Table 1), of the low beta (16 Hz) with respect to gamma band (64 Hz) existed. On the other
247 hand, when considering the core-periphery structure, the beta and gamma rhythms (16 Hz, 32 Hz, 64 Hz)
248 showed an increase with respect to the delta and theta rhythms (2 Hz, 4 Hz), see Figure 5a and
249 Supplementary Table 2. We additionally found another weakly significant increase of core-periphery
250 community interactions between 2 Hz and 8 Hz (p = 0.042, see Supplementary Table 2).

9
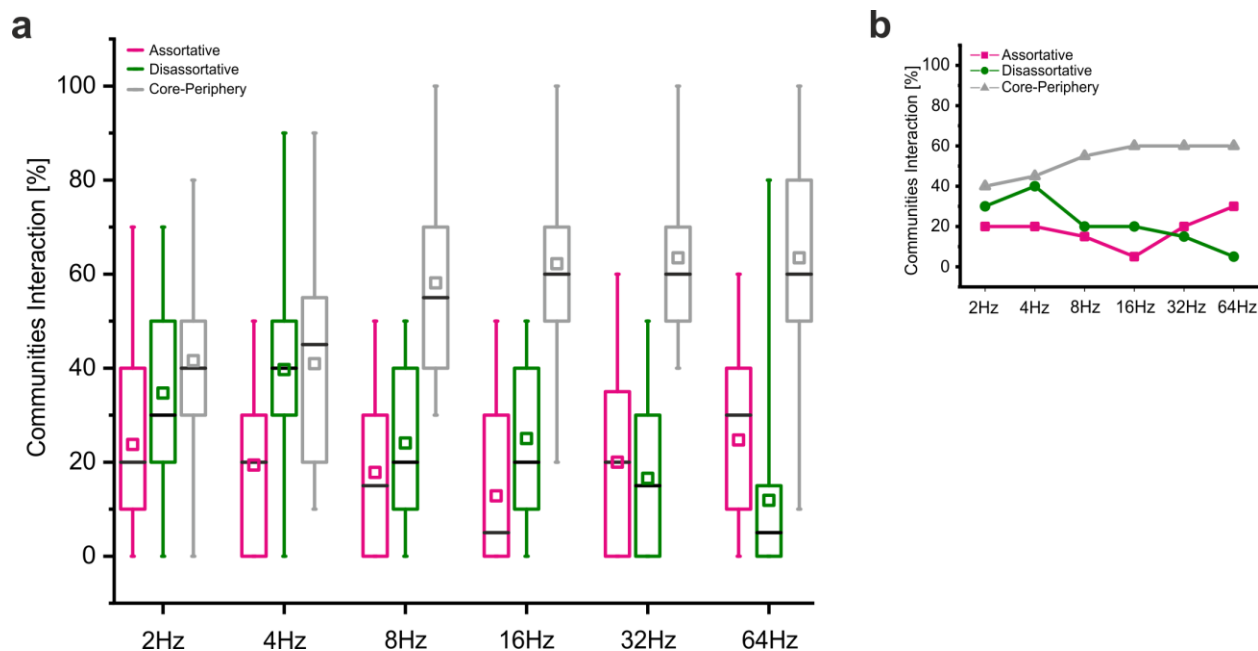
Fig. 5. Organization of the meso-scale structure in the time-frequency domain. a Boxplots representing distributions across participants of the three meso-scale classes for each carrier frequency. Magenta: assortative; green: disassortative; gray: core-periphery. Boxplots show upper and lower bound of the distributions at 25th and 75th percentile. Whiskers indicate the 1st and 99th percentile. The black horizontal lines represent the median, while the small colored squares indicate the mean of the distributions. Statistical analysis for multiple comparisons across carrier frequencies of the depicted data is reported in Table 1 and Table 2 in the Supplementary Materials. **b** Median values of each meso-scale structure distributions (black horizontal lines in a) across frequency bands.

Overall, we observed complementary trends along the entire range of oscillatory rhythms (i.e. delta and theta vs. gamma). Specifically, for increasing frequencies we found respectively a decreasing disassortative and an increasing core-periphery trend (see Figure 5b). This phenomenon was not observed for low frequencies (i.e. alpha). Finally, we averaged across participants the total amount of meso-scale modalities and we then overlaid these values onto the T1-weighted template (see Figure 6). We observed that the core-periphery structure was predominant starting from alpha/beta bands and peaking in low and high gamma bands. The prefrontal and PTO areas showed the highest degree of core-periphery (see Figure 6 and Supplementary Figure S4) and this was true also when progressively moving towards higher-frequency oscillations. In addition, the medial areas belonging to limbic system showed a low degree of core-periphery in the higher rhythms. When considering the lowest delta/theta bands the core-periphery pattern decreased its overall amount. This decrease in core-periphery organization corresponded to an emerging role of the disassortative structure. Despite this increase, the amount of disassortative and core-periphery was still comparable. Concerning the disassortative structure, there was a spatial gradient increasing from anterior-medial to posterior areas emerging in the alpha and beta band. Instead, the opposite gradient (i.e. increasing in posterior-anterior direction) was found for the core-periphery structure, in the same bands.

Fig. 6. Mean community classes across participants in the frequency domain. Each column indicates the meso-scale class (assortative, disassortative, core-periphery) while each row indicates the carrier frequency (2 Hz, 4 Hz, 8 Hz, 16 Hz, 32 Hz, 64 Hz). The colorbar is kept fixed to the minimum and maximum values across the meso-scale modalities. See Figure S4 in the Supplementary Materials where the same plot is showed with colorbar customized between minimum and maximum values within each meso-scale modality.

Discussion

To date, the features of human brain meso-scale structure during resting state have not been fully explored. Specifically, the meso-scale spectral fingerprints are still unknown and evidences about how the diversity of meso-scale structure (i.e. assortative, disassortative and core-periphery) organizes over the frequency spectrum are missing. Thus, we aimed at filling this knowledge gap, by using WSBM to infer the richness of the latent community structure estimated from source-reconstructed hdEEG signals. We indeed described the spatial distribution of communities and their interactions across time and frequency domains. Our analysis showed that the meso-scale is characterized by a frequency-specific organization. We highlighted that community structure in the frequency domain is characterized by a high level of non-assortativity. Finally, we found that association areas exhibited the highest degree of integration, as revealed by the high incidence of core-periphery structure for those areas.

Parameter selection in the time domain

To the best of our knowledge, no previous hdEEG study has been conducted to investigate WSBM community detection. We thus shaped our analysis on an already published procedure on Blood Oxygenation Level Dependent (BOLD) signals oscillations, where the authors fitted the WSBM to group-representative adjacency matrix (*5*). Thus, we performed the parameter selection procedure in the time domain and we kept the chosen best K in the frequency domain to compare the community detection results in different frequency bands. One may argue that the time domain is affected by the problem of volume conduction (*33*). However, many approaches have been proposed to attenuate such effect for electrophysiological recordings (for a review, see (*34*)). Among all, we applied spatial filtering during sources reconstruction, which mitigates the negative effects of volume conduction on FC (*34*). Indeed, we employed spatial filtering for the analysis in the time domain, whereas, for spectral analysis, we combined

11

304 both spatial filtering and the method of power spectra orthogonalization (*27*), which has been largely
305 accepted and validated (*35*) even by recent studies employing both low and high density montages (*17, 26,*
306 *29, 36*). Moreover, time domain analysis is a valid tool to estimate the K_{best} and for the further comparisons
307 of the meso-scale structure in the frequency domain, because the time-courses of source-reconstructed
308 hdEEG signals contain all the neuronal oscillations of interest, that are then band-pass filtered during
309 spectral analysis.

310 According to the above, we performed parameter selection in the time domain. The goal of parameter
311 selection in a community detection problem is to find models which have to be simultaneously simple and
312 good at describing the system (*11*). We thus aimed at identifying a fine grain parcellation while maintaining
313 a steady clustering performance, as indicated by low NVI value. We therefore selected $K_{best} = 5$. Indeed,
314 higher number of modules (i.e. $K \geq 6$) showed weak reliability of the clustering performance, which may
315 have led to the calculation of a non-representative community assignment. Finally, the same number of
316 communities was employed to describe meso-scale organization with other neuroimaging datasets (*5*).

Meso-scale structure has frequency-dependent fingerprints

318 By relying on the spectral richness of hdEEG recordings, we could investigate how meso-scale and the
319 related way to route information within the FC network, is organized across frequency bands. According
320 to our results, the meso-scale structure clearly indicates a frequency-dependent behavior. Indeed, when
321 increasing the neuronal oscillation frequency from delta to high gamma, the core-periphery structure
322 increased, showing greater values in the gamma band. Conversely, the disassortative structure showed an
323 opposite trend when compared to core-periphery, as disassortative organization exhibited high values in
324 delta and theta rhythms. In addition, the assortative structure was uniformly distributed across the spectrum
325 and did not show any particular trend. Thus, in the low frequency bands, characterized by long-range
326 communication (*37*), information is exchanged across long-distances. This behavior is, in our opinion, well-
327 expressed by the disassortative structure which is significantly higher in delta and theta when compared to
328 the other frequencies, thus favoring high information flow between distinct modules (*10*). Therefore, we
329 can consider the disassortative structure as a meso-scale fingerprint of the long-distance and slow
330 oscillations. However, in these low rhythms even the core-periphery structure is comparable with the
331 disassortative one, suggesting a 'hybrid' communication mechanism during resting state. Moreover, at low
332 frequencies, the clustering in separate and functionally distinct areas is less clear than the higher frequency
333 bands, because these oscillatory regimens are characterized by long-range interactions (*37*) which require
334 communication among several different areas. On the other hand, by increasing the oscillatory frequency
335 (from delta to low and high gamma band) we encountered not only an increase of the core-periphery meso-
336 scale structure, but also a clearer subdivision in functional clusters with respect to the low and mid-low
337 bands (see Figure 4) that, in turn, may reflect a local processing of information. In fact, gamma oscillations
338 might represent a rhythmic synaptic inhibition mediated by parvalbumin-expressing inhibitory interneurons
339 and the interconnected pyramidal neurons (*38-40*). Gamma-oscillations might thus resemble a local
340 processing of coactive functional areas. Indeed, these functional areas are approximately grouped in the
341 five modules emerging at 32 and 64 Hz: sensory associative, somatomotor, executive, limbic and visual.
342 Other studies showed that neuronal oscillations in the gamma band reflect not only a local processing, but
343 also synchronization across long-distance areas (*38, 41*). From this perspective, the core-periphery structure
344 might be a good candidate to support this "dual property" of gamma oscillations: the dense core represents
345 the local processing, while the numerous interactions between the core and the nodes located in the
346 peripheries may indicate the presence of the long-distance connections that are also typical of gamma
347 oscillations (*39*). In summary, we provided evidence supporting the concept that non-assortative structures
348 reflect how information is processed in the delta/theta (disassortative) and gamma (core-periphery) bands.

349 Furthermore, despite the considerable amount of disassortative and core-periphery structures at specific
350 frequencies, we must recall that a certain degree (around 20 % of median values) of assortative structure is
351 still present and uniformly distributed across the frequency spectrum. According to previous fMRI studies,
352 the brain presents a mixed meso-scale organization, but the network dominantly exhibits
353 modular/assortative meso-scale structures, specifically during resting state (*5, 10*) and, to a lesser extent,
354 during cognitive tasks (*10*). Our hdEEG analysis showed that the meso-scale assortative structure is
355 predominant in the time domain, thus confirming previous findings (see Figure 3). Instead, in the frequency
356 domain the amount of assortative modules was reduced, and a clear non-assortative organization emerged.

357 **Association cortex underlie core-periphery structures**

358 We observed a whole-brain high incidence of core-periphery structure towards the higher-frequency bands,
359 starting from alpha oscillations. In this overall level of increased core-peripheriness, high-order association
360 areas belonging to prefrontal and PTO cortices emerged among others. High levels of non-assortativity
361 have been linked to association areas using fMRI (*10*). We found that, when decreasing the carrier
362 frequency, the meso-scale organization changed: there was still a considerable amount of core-periphery,
363 but the disassortative structure increased, exhibiting a spatially distributed gradient in the middle bands (i.e.
364 alpha, beta) from posterior to anterior cortices. On the other hand, the prefrontal cortices were strongly
365 core-periphery. When the frequencies are further decreased, in delta and theta bands, we had the steepest
366 decrease of core-periphery, favoring an increasing of the disassortative structure (particularly in the medial
367 frontal and temporal areas) that might underlie spatially distributed information processing (see above).
368 Overall, the regions selectively exhibited a frequency-specific behavior, in particular when comparing low
369 (delta/theta) and high rhythms (gamma). Association areas such as PTO showed high degree of core-
370 peripheriness across frequency bands, corroborating the integrative role of this meso-scale modality. On
371 the other hand, medial frontal areas exhibited both high degree of core-periphery in the higher bands while
372 higher level of disassortativity in the lower bands. We therefore posit that the same regions might employ
373 a specific frequency to route information, underlying a frequency-dependent meso-scale organization that
374 is also linked to the cortical and subcortical spatial distribution.

375 Our analysis allowed, for the first time, to observe WSBM-estimated meso-scale organization with a
376 different focus: by investigating FC in different frequency bands, we captured peculiar features of module
377 interactions revealing the non-assortative nature of resting state networks, demonstrating its frequency-
378 specificity. Furthermore, this study demonstrated that WSBM applied to sources-level neuronal oscillations
379 is an effective tool to explore yet unknown properties of FC topological organization.

380 Overall, these results may be taken into consideration for future studies that will address the
381 pathophysiological mechanisms underlying neurological/psychiatric disorders (*16, 42*). It would indeed be
382 crucial to examine how the presence of a neurological disease can affect the meso-scale structure and
383 whether and how a neurorehabilitation program can impact the re-organization of brain networks and the
384 interactions among communities. This will have a direct impact in the clinical assessment of sensory, motor
385 and cognitive functions, being EEG acquisitions widely employed in the clinical setting. Collectively, the
386 results of our study increase the knowledge of human brain meso-scale organization and of communication
387 modalities between brain networks, which is still an open topic in network neuroscience (*6*).

388

389

Materials and Methods

Participants

We recruited 32 healthy volunteers (29.6 ± 4.5 years, mean ± SD, 17 females). To be included, the participants had: *a)* to be right-handed according to the Edinburgh inventory (*43*); *b)* to be without neurological or psychiatric disorders; *c)* to have normal or corrected-to-normal vision; *d)* to be free of psychotropic and/or vasoactive medication. Prior to the experimental procedure, all participants provided written informed consent. The study, which was in line with the standard of the Declaration of Helsinki, was approved by the local ethical committee (CER Liguria Ref. 1293 of September 12th, 2018).

Resting state hdEEG recording and MRI acquisition

HdEEG signals were recorded using a 128-channel amplifier (ActiCHamp, Brain Products, Germany) while participants were comfortably sitting with their eyes open fixating on a white cross on a black screen for five minutes. Participants were required to relax as much as possible and to fixate on the cross, located in the middle of a screen in front of them. The experiment was performed according to the approved guidelines, in a quiet, air-conditioned laboratory with soft natural light. HdEEG signals were collected at 1000 Hz sampling frequency, using the electrode FCz (over the vertex) as physical reference electrode. The horizontal and vertical electrooculograms (EOG) were collected from the right eye for further identification and removal of ocular-related artifacts. Prior to resting state hdEEG recordings, the three-dimensional locations of the 128 electrodes on the scalp were collected with either infrared color-enhanced 3D scanner (*44*) or Xensor digitizier (ANT Neuro, The Netherlands). To build each participant's high-resolution head model, the participants underwent T1-weighted MRI acquisition using either a 3 T (N = 28) or a 1.5 T (N = 4) scanner (see Suppl. Materials for details about acquisition parameters).

Pre-processing of hdEEG recordings

HdEEG preprocessing was performed according to the same steps described in previous works (*17, 18*). Briefly, we first attenuated the power noise in the EEG channels by using a notch filter centered at 50 Hz. Later, we identified channels with low signal to noise ratio by following an automatic procedure. We combined information from two channel-specific parameters: i) the minimum Pearson correlation between a channel against all the others in the frequency band of interest (i.e. 0.5-100 Hz); ii) the noise variance that we defined in a band where the EEG information is negligible (i.e. 200-250 Hz). We defined a channel as "bad", whenever one of the two parameters described above were outliers as compared to the total distribution of values. We interpolated the identified bad channels with the information of the neighboring channels, using Field Trip (http://www.fieldtriptoolbox.org/). Then, hdEEG signals were band pass filtered (0.5-100 Hz) with a zero-phase distortion FIR filter and downsampled to 250 Hz. To further reduce noise in our data, we employed the fast-ICA algorithm (http://research.ics.aalto.fi/ica/fastica/) to identify independent components related to ocular and movement artifacts. To classify the ocular artifacts we used the following parameters: i) Pearson correlation between the power of the independent components and the vertical and horizontal EOG; ii) the coefficient of determination obtained by fitting the independent component (IC) spectrum with a 1/f function. We classified the IC as ocular artifacts if at least one of the two parameters was above a pre-defined thresholds (0.2 and 0.5, as in (*18*)). Finally, for movement-related artifacts, we used the kurtosis of the independent component (we considered a kurtosis exceeding the value

14

431 of 20 (*18*) indicated a noisy IC). We re-referenced the artifacts-free signals with the average reference
432 approach (*45*).

433

Head model of volume conduction and source reconstruction

435 We followed the same procedure as detailed in (*29*). Briefly, we used T1-weighted structural images in
436 order to generate a realistic volume conductor model. In accordance with previous studies (*17, 18*), we
437 assigned conductivity values to 12 tissue classes (skin, eyes, muscle, fat, spongy bone, compact bone, gray
438 matter, cerebellar gray matter, white matter, cerebellar white matter, cerebrospinal fluid and brainstem),
439 based on the literature (see Liu et al. (*18*) for the conductivity values assigned per each tissue class). Then,
440 given the intrinsic difficulty in segmenting all the 12 classes directly on the T1-weighted individual space,
441 we warped the MNI (Montreal Neurological Institute) template to individual space using the normalization
442 tool of SPM12 (http://www.fil.ion.ucl.ac.uk/spm/software/spm12), as reported in Liu et al. (*18*). Then, we
443 spatially co-registered the 128 electrodes positions onto each individual T1-weighted space. We
444 approximated the volume conduction model using a finite element method (FEM) and, to estimate the
445 relationship between the measured scalp potentials and the dipoles corresponding to brain sources, we
446 employed the Simbio FEM method (https://www.mrt.uni-jena.de/simbio/). Finally, by combining the
447 individual head model conductor and the artifacts-free hdEEG signals, we reconstructed source activity
448 using the eLORETA (*46*) algorithm. Sources were constrained within a 6 mm regular grid covering the
449 cerebral gray matter. Thus, we reconstructed the sources (voxels) per each participant and we then mapped
450 the voxels time courses into 384 regions of interest (ROIs) of the AICHA atlas (*30*). This procedure defines
451 the nodes for the subsequent meso-scale structure investigation. We estimated the activity of each ROI
452 employing the first principal component of the voxels falling within a sphere centered in the ROI center of
453 mass and with 6 mm radius.

454

Spectral analysis

456 We implemented time-frequency analysis by convolving the ROIs signals (X_i(t), with i = 1..N) with
457 Generalized Morse Wavelets (GMW), described in (*47*). This wavelet superfamily guarantees, under certain
458 parametrizations, a strict analytic behavior and therefore is appropriate for accurate time-frequency
459 analysis. The GMW is defined, in the frequency domain, as:

460 $$\psi_{\beta,\gamma}(f) = a_{\beta,\gamma} f^\beta e^{-f^\gamma}$$

461 Where, $a_{\beta,\gamma} = 2(e\gamma/\beta)^{\beta/\gamma}$ is a normalizing constant, f are the carrier frequencies of the wavelet, and β
462 and γ are the two parameters controlling the wavelet shape. As suggested in (*47*), a choice of γ = 3,
463 guarantees the most symmetric, most nearly Gaussian, and generally most frequency concentrated member
464 of the GMW superfamily. In this work, we thus set γ = 3.00 and β = 11.33 to capture the essential idea of
465 the widely used Morlet wavelet (*27*), while avoiding aliasing for specific parameter choices (*47*). We used
466 23 carrier frequencies, ranging from $2^{0.5}$ to 2^6 Hz in quarter steps (f = $2^{(0.5:0.25:6)}$ Hz), to cover a large part
467 of the EEG spectrum with a fine detail. We employed the Matlab version of the Jlab toolbox (freely
468 available online: http://www.jmlilly.net/jmlsoft.html).

469

470

Functional connectivity analysis in the time domain

471   We defined the single-subject FC matrix ($ADJ_S^T, 384 \times 384, S = 1..32$) using the Pearson's correlation
472   coefficient (r) between the time course of each pair of ROIs. Then, to explore FC in the time domain, we
473   averaged single-subject's adjacency matrices and we regressed out the effect of the Euclidean distance
474   between the ROIs since we considered the Euclidean distance as a covariate of no interest, as performed in
475   Betzel et al. (5) We obtained a group level representative matrix (ADJ_G^T) whose elements (i.e. the weights)
476   contained the strength of the connection between brain regions. We Fisher-transformed (arctanh(ADJ_G^T))
477   the resulting correlation values of the group-representative FC matrix to improve Gaussianity. Finally, we
479   linearly mapped ADJ_G^T values between the [-1, +1] range, obtaining:

$$ADJ^T = b_1 + (\frac{(val - a_1)(b_2 - b_1)}{(a_2 - a_1)})$$

481   Where val is a single element of ADJ_G^T; a_1, a_2 are the minimum and maximum edges value of ADJ_G^T; b_1, b_2
482   are the limits of the new range -1 and +1. This linear transformation allows for further comparison of the
483   meso-scale structure among different frequency content (see next section *cf.* '*Functional connectivity in the*
484   *frequency domain*'). It is indeed necessary to normalize the weights of the adjacency matrices in the same
485   range to compare outputs of the WSBM, according to the literature (12).

486

Functional connectivity analysis in the frequency domain

488   To measure the frequency-specific properties of FC, we employed the method of power envelope
489   orthogonalization (27) that is necessary in order to estimate the pairwise connection strength among the
490   ROIs. Indeed, although the brain activity estimation at the sources level is a promising tool to investigate
491   the brain dynamics at both good spatial and high temporal resolutions, it is affected by the signal leakage
492   problem (26, 27). Reconstructing cortical and sub-cortical sources (several thousand sources) from scalp
493   potentials (here 128 electrodes) is an ill-posed inverse problem, introducing artefactual cross-correlations
494   between sources. A recent validation study (35) established the power envelope orthogonalization as a valid
495   candidate to estimate the physiological FC properties in the field of neuroimaging by electrophysiological
496   recordings. Thus, for each wavelet carrier frequency and participant, we followed the same
497   orthogonalization procedure, described in previous EEG studies (17, 26), leading to the estimation of
498   $ADJ_S^F(f)$ ($f = 2^{(0.5:0.25:6)}$; $S = 1..32$). The group-representative adjacency matrices ($ADJ^F(f)$) were
499   obtained starting from the single subject adjacency matrices $ADJ_S^F(f)$ and performing the same procedure
500   described for the time domain (*cf.* 'Functional connectivity analysis in the time domain'). The same
501   regressing and mapping procedures were also implemented for the analysis of single subject adjacency
502   matrices that were employed to calculate the percentage of each community interaction.

503

Community detection via Weighted Stochastic Block Models

505   WSBM is as an unsupervised learning algorithm for the identification of network communities that group
506   together network nodes that have similar FC patterns (12). The WSBM can work without the need of
507   thresholding the adjacency matrix, as this procedure might have a negative impact on the analysis of the
508   meso-scale structure of network connectivity, as previously reported (12). The WSBM goal is to learn the
509   hidden community structure that is estimated from both the existence and the weights of edges. Moreover,
510   an interesting property is that the algorithm retains the principle of stochastic equivalence, that is, all the
511   nodes in a community have the same probability of being connected with all the remaining communities of

16

512 the network. This last property is important in differentiating this community detection problem from the
513 modularity maximization algorithms that are extensively employed for community detection in network
514 neuroscience and are by nature biased towards the assortative community structure. Additionally, it is
515 important to note that stochastic block-modelling has the unmet advantage of being a generative model, as
516 it tries to estimate the process underlying the observed network topology. The WSBM learns two
517 parameters starting from the adjacency matrix (in this section, for general explanation, we refer to any
518 adjacency matrix, being it either in time or frequency domain or obtained by single or group level, by using
519 the notation ADJ) and from a priori assumptions about the distributions of edges weights and existence of
520 edges. An important parameter is the vector of nodes assignment $Z = [z_1, \dots, z_N]$ where $z_j \in \{1, \dots, K\}$, with
521 N the number of nodes and K the number of communities the algorithm must learn. The other parameter is
522 the edge bundle matrix (or affinity matrix) θ ($[K \times K]$), representing the probability of two communities
523 being connected. It is worth noting that the probability of connection between two nodes only depends on
524 their community labels assignment, $p_{ij} = \theta_{z_i z_j}$. In its formulation, the log-likelihood of the adjacency
525 matrix being described by the parameters θ and Z, can be written as (*5, 12*):

526
$$\log[p(ADJ|Z,\theta)] = \alpha \left[\sum_{ij} T_e(ADJ_{ij})\eta_e\left(\theta_{z_i z_j}^{(e)}\right) \right] + (1-\alpha) \left[\sum_{ij} T_w(ADJ_{ij})\eta_w\left(\theta_{z_i z_j}^{(w)}\right) \right]$$

527 where α is a tuning parameter that combines the contribution of the two summations, which respectively
528 model edges weights and edges existence, to infer the latent community structure. $T_e(ADJ_{ij}), \eta_e\left(\theta_{z_i z_j}^{(e)}\right)$ and
529 $T_w(ADJ_{ij}), \eta_w(\theta_{z_i z_j}^{(w)})$ are the sufficient statistics and the natural parameters of the exponential family
530 describing the distributions of the edges existence (T_e, η_e) and the edges weights (T_w, η_w). Lastly, i, j
531 indicate the edges of the adjacency matrix onto which we inferred the latent community structure. Usually,
532 when applying the WSBM framework to structural and functional brain networks, the edges existence and
533 weights are drawn from Bernoulli and Normal distributions (*5, 10, 13, 14*), respectively. In our case, α is
534 set to zero because the graph is fully connected (i.e. no thresholding applied) and, thus, we did not need to
535 model the edges existence. Hence, our likelihood maximization is simplified leading to a pure-WSBM (*12*)
536 (pWSBM) that learns from the weights information, that are assumed to be normally-distributed between
537 communities. The remaining issue is to find a reliable estimation of the posterior distribution, i.e.
538 $p(Z, \theta|ADJ)$ that has no explicit analytic formulation (*12*). To this purpose, we made use of the code freely
539 available here (http://tuvalu.santafe.edu/~aaronc/wsbm/). The code finds an approximation of the posterior
540 probability using a Variational Bayes (VB) approach. VB provides a solution to approximate the unknown
541 posterior distribution by transforming an inference problem into an optimization problem. The algorithm
542 minimizes the Kullback-Lieber divergence D_{KL} (*48*) to the posterior probability (for further information
543 about D_{KL} applied to WSBM, see (*12*). The solution proposed by (*12*) states that minimizing the D_{KL} is
544 equivalent to maximize the evidence lower bound of the model marginal log-likelihood (logEvidence),
545 $p(ADJ|Z, \theta)$. Thus, the best approximation of the posterior is obtained through a procedure aimed at
546 maximizing the logEvidence score. Thus, if the logEvidence is maximized, the D_{KL} is the closest possible
547 to the posterior distribution, $p(Z, \theta|ADJ)$. After properly initializing the priors for θ and z the VB algorithm
548 takes the best (i.e. the greatest) logEvidence value across multiple independent trials (or restarts) of the
549 algorithm. We choose a maximum of 100 independent trials to find the best logEvidence value. Within this
550 limit, the algorithm searches for the best logEvidence value. At each trial, the initial probability of a node
551 being assigned to a community is randomized. Every time a better logEvidence value (i.e. a better solution)
552 is obtained, the algorithm updates the solution. We selected the communities assignment in correspondence
553 of the highest logEvidence value. We run the WSBM model for different values of K and we performed a

554 parameter selection procedure to infer the best number of K communities for our dataset, as described in
555 the next section.

556

Parameter selection: optimal number of communities

558 The main idea behind our parameter selection procedure is to look at the stability of the clustering
559 performance, i.e. the aim was to find the best number of communities K for which the clustering
560 performance is as stable as possible. As a first step towards this goal, we performed 200 WSBM fits, each
561 one consisting of a maximum of 100 independent trials, on the group level adjacency matrix computed in
562 the time domain (ADJ^T, full bandwidth). We calculated 200 WSBM fits for different values of K (ranging
563 from 2 to 16). To evaluate the clustering performance, we calculated the Normalized Variation of
564 Information (*31*) (NVI) across each pair of fits. We averaged across the fits selecting the best K-values
565 corresponding to the smallest NVI values. Indeed, the lower the NVI the more stable is the clustering
566 performance. To further validate our choice, we also checked the cluster performance by using two other
567 metrics: the Adjusted Rand Index (*32*) (ARI) and the Normalized Mutual Information (*31*) (NMI). For these
568 metrics, a consistent matching between couple of fits corresponds to NMI = 1 and to ARI = 1. With this
569 parameter selection procedure, we obtained the best number of communities and we used it to investigate
570 the meso-scale structure in both time and frequency domains (at both group and single subject level).

571

Community assignment in the time and frequency domain: central fit

573 Once we defined the best number of communities at the group level (K_{best}), we needed to choose the best
574 nodes assignment among the 200 fits. Therefore, we used the community assignment corresponding to the
575 central fit across the 200 fits. We defined the central fit as the fit whose distance is minimized from all the
576 others fits using the NVI, as in a previous work (*13*) (we used the function *partition_distance.m* of the Brain
577 Connectivity Toolbox (*49*)). We used the central fit not only to identify and to show the resulting
578 communities at the group level, but also for all the subsequent steps of our analysis: the investigation of
579 how the percentage of between-community interactions varies across frequencies. Indeed, in addition to fit
580 the WSBM generative model with the group level time domain (ADJ^T) and frequency domain (ADJ^F)
581 matrices, we also fitted the model for K = K_{best} at the single-subject level (ADJ_S^T and ADJ_S^F): for each
582 participant we thus performed 100 WSBM fits and we selected as best fit the central one, employing NVI,
583 as for the group level. The central fit was calculated both for the time domain (ADJ_S^T) and six carrier
584 frequencies ($ADJ_S^F(f)$, f = 2 Hz, 4 Hz, 8 Hz, 16 Hz, 32 Hz, 64 Hz). These carrier frequencies have been
585 chosen as a subset of those selected in previous studies (*26, 27*). Note that due to high computational cost,
586 we performed the latter frequency-domain analysis across 100 fits.

587

Characterizing the meso-scale structure: between-community interactions

589 At the single-subject level, we investigated how pairs of communities interacted with each other in order
590 to generate assortative, disassortative and core-periphery architecture. This permitted us to investigate the
591 between-community interactions in both time and frequency domains. For each pair of communities r and
592 s, we estimated the within- and between- community density (*10*), a topological property of the detected
593 modules (*9*):

594 $\omega_{rr} = \frac{1}{N_r N_r}\sum_{x\in r}\sum_{y\in r} ADJ_{S,xy};$ $\omega_{cc} = \frac{1}{N_c N_c}\sum_{x\in c}\sum_{y\in c} ADJ_{S,xy};$ $\omega_{rc} = \frac{1}{N_r N_c}\sum_{x\in r}\sum_{y\in c} ADJ_{S,xy};$

595   Where, N_r and N_c are the number of nodes assigned to the communities r and c at the central fit. We

596   calculated community density for the time domain ADJ_S^T and for the different frequencies $ADJ_S^F(f)$ at the

597   K_{best}. Then, the between-community interactions fall into one of the three categories as reported in (*5, 10*),

598   according to the following criteria:

599

$$M_{rc} = \begin{cases} M_{assortative} & \text{if } \min(\omega_{rr}, \omega_{cc}) > \omega_{rc} \\ M_{core-periphery} & \text{if } \omega_{rr} > \omega_{rc} > \omega_{cc} \text{ or } \omega_{cc} > \omega_{rc} > \omega_{rr} \\ M_{disassortative} & \text{if } \omega_{rc} > \max(\omega_{rr}, \omega_{cc}) \end{cases}$$

600   We calculated the percentage of between-community interactions for each participant with respect to the

601   total number of possible interactions, corresponding to $\frac{1}{2}[K_{best} \cdot (K_{best} - 1)]$. Then, we averaged the

602   percentage across all participants for the time domain and for the six carrier frequencies.

603

Statistical analysis of between-community interactions

605   Our working hypothesis is to understand whether the meso-scale connectivity organizes across frequency

606   bands, i.e. the meso-scale connectivity has frequency-specific features. Prior to testing this hypothesis, we

607   performed statistical testing to check how meso-scale arranges in the time domain. Given the non-normality

608   of the distributions, we employed non-parametric tests. We used the Kruskal-Wallis test to examine whether

609   the meso-scale structure shows a statistically significant effect of the between-community classes. Then,

610   we employed a post-hoc comparison of mean ranks as implemented in Statistica 13 software package

611   (StatSoft Inc., Tulsa) to investigate potential differences among the three interaction classes. For the

612   frequency analysis, we also performed a set of Kruskal-Wallis tests to verify for each interaction class (i.e.

613   assortative, disassortative and core-periphery) whether the carrier frequency has a statistically significant

614   effect. Finally, a post-hoc comparison of mean ranks has been used to further highlight the potential

615   differences among the six carrier frequencies within each community class.

616

617

19

References

1. K. J. Friston, Functional and effective connectivity: a review. *Brain Connect* **1**, 13-36 (2011).

2. A. T. Reid *et al.*, Advancing functional connectivity research from association to causation. *Nature Neuroscience* **22**, 1751-1760 (2019).

3. R. F. Betzel, D. S. Bassett, Multi-scale brain networks. *Neuroimage* **160**, 73-83 (2017).

4. M. N. Hallquist, F. G. Hillary, Graph theory approaches to functional network organization in brain disorders: A critique for a brave new small-world. *Netw Neurosci* **3**, 1-26 (2019).

5. R. F. Betzel, J. D. Medaglia, D. S. Bassett, Diversity of meso-scale architecture in human and non-human connectomes. *Nat Commun* **9**, 346 (2018).

6. O. Sporns, Graph theory methods: applications in brain networks. *Dialogues Clin Neurosci* **20**, 111-121 (2018).

7. K. Glomb *et al.*, Using structural connectivity to augment community structure in EEG functional connectivity. *bioRxiv*, 831743 (2019).

8. M. E. J. Newman, Modularity and community structure in networks. *P Natl Acad Sci USA* **103**, 8577-8582 (2006).

9. J. O. Garcia, A. Ashourvan, S. F. Muldoon, J. M. Vettel, D. S. Bassett, Applications of Community Detection Techniques to Brain Graphs: Algorithmic Considerations and Implications for Neural Function. *P Ieee* **106**, 846-867 (2018).

10. R. Betzel, M. A Bertolero, D. Bassett, *Non-assortative community structure in resting and task-evoked functional brain networks*. (2018).

11. S. Fortunato, Community detection in graphs. *Phys Rep* **486**, 75-174 (2010).

12. C. Aicher, A. Jacobs, A. Clauset, *Learning Latent Block Structure in Weighted Networks*. (2014), vol. 3.

13. J. Faskowitz, X. Yan, X. N. Zuo, O. Sporns, Weighted Stochastic Block Models of the Human Connectome across the Life Span. *Sci Rep* **8**, 12997 (2018).

14. J. Faskowitz, O. Sporns, Mapping the community structure of the rat cerebral cortex with weighted stochastic block modeling. *Brain Structure and Function*, 1-14 (2019).

15. D. M. Pavlovic, P. E. Vertes, E. T. Bullmore, W. R. Schafer, T. E. Nichols, Stochastic blockmodeling of the modules and core of the Caenorhabditis elegans connectome. *PLoS One* **9**, e97584 (2014).

16. M. Siegel, T. H. Donner, A. K. Engel, Spectral fingerprints of large-scale neuronal interactions. *Nat Rev Neurosci* **13**, 121-134 (2012).

17. J. Samogin, Q. Liu, M. Marino, N. Wenderoth, D. Mantini, Shared and connection-specific intrinsic interactions in the default mode network. *Neuroimage* **200**, 474-481 (2019).

18. Q. Y. Liu, S. Farahibozorg, C. Porcaro, N. Wenderoth, D. Mantini, Detecting Large-Scale Networks in the Human Brain Using High-Density Electroencephalography. *Hum Brain Mapp* **38**, 4631-4643 (2017).

19. M. Seeber *et al.*, Subcortical electrophysiological activity is detectable with high-density EEG source imaging. *Nature Communications* **10**, (2019).

20. A. Coito *et al.*, Altered directed functional connectivity in temporal lobe epilepsy in the absence of interictal spikes: A high density EEG study. *Epilepsia* **57**, 402-411 (2016).

21. S. Waninger *et al.*, Neurophysiological Biomarkers of Parkinson's Disease. *Journal of Parkinson's Disease*, 1-10 (2020).

22. R. Cassani, M. Estarellas, R. San-Martin, F. J. Fraga, T. H. Falk, Systematic Review on Resting-State EEG for Alzheimer's Disease Diagnosis and Progression Assessment. *Dis Markers* **2018**, 5174815 (2018).

23. A. Damborská *et al.*, Altered directed functional connectivity of the right amygdala in depression: high-density EEG study. *Scientific Reports* **10**, 1-14 (2020).

24. B. He, A. Sohrabpour, E. Brown, Z. M. Liu, Electrophysiological Source Imaging: A Noninvasive Window to Brain Dynamics. *Annu Rev Biomed Eng* **20**, 171-196 (2018).

668 25. N. Coquelet *et al.*, Comparing MEG and high-density EEG for intrinsic functional connectivity
669   mapping. *NeuroImage*, 116556 (2020).
670 26. M. Siems, A. A. Pape, J. F. Hipp, M. Siegel, Measuring the cortical correlation structure of
671   spontaneous oscillatory activity with EEG and MEG. *Neuroimage* **129**, 345-355 (2016).
672 27. J. F. Hipp, D. J. Hawellek, M. Corbetta, M. Siegel, A. K. Engel, Large-scale cortical correlation
673   structure of spontaneous oscillatory activity. *Nat Neurosci* **15**, 884-890 (2012).
674 28. F. de Pasquale, M. Corbetta, V. Betti, S. Della Penna, Cortical cores in network dynamics.
675   *Neuroimage* **180**, 370-382 (2018).
676 29. R. Iandolo *et al.*, Small-World Propensity Reveals the Frequency Specificity of Resting State
677   Networks. *IEEE Open Journal of Engineering in Medicine and Biology*, (2020).
678 30. M. Joliot *et al.*, AICHA: An atlas of intrinsic connectivity of homotopic areas. *J Neurosci Methods*
679   **254**, 46-59 (2015).
680 31. M. Meila, Comparing clusterings - an information based distance. *J Multivariate Anal* **98**, 873-895
681   (2007).
682 32. L. Hubert, P. Arabie, Comparing Partitions. *J Classif* **2**, 193-218 (1985).
683 33. G. L. Colclough, M. J. Brookes, S. M. Smith, M. W. Woolrich, A symmetric multivariate leakage
684   correction for MEG connectomes. *Neuroimage* **117**, 439-448 (2015).
685 34. M. X. Cohen, Analyzing Neural Time Series Data: Theory and Practice. *Iss Clin Cogn Neurop*, 1-
686   578 (2014).
687 35. M. Siems, M. Siegel, Dissociated neuronal phase- and amplitude-coupling patterns in the human
688   brain. *Neuroimage* **209**, 116538 (2020).
689 36. R. L. van den Brink *et al.*, Task-free spectral EEG dynamics track and predict patient recovery
690   from severe acquired brain injury. *Neuroimage Clin* **17**, 43-52 (2018).
691 37. A. T. Leong *et al.*, Long-range projections coordinate distributed brain-wide neural activity with a
692   specific spatiotemporal profile. *Proc Natl Acad Sci U S A* **113**, E8306-E8315 (2016).
693 38. V. S. Sohal, How close are we to understanding what (if anything) γ oscillations do in cortical
694   circuits? *Journal of Neuroscience* **36**, 10489-10495 (2016).
695 39. V. S. Sohal, Insights into cortical oscillations arising from optogenetic studies. *Biological
696   psychiatry* **71**, 1039-1045 (2012).
697 40. G. Buzsaki, N. Logothetis, W. Singer, Scaling brain size, keeping timing: evolutionary preservation
698   of brain rhythms. *Neuron* **80**, 751-764 (2013).
699 41. G. Buzsáki, E. W. Schomburg, What does gamma coherence tell us about inter-regional neural
700   communication? *Nature neuroscience* **18**, 484 (2015).
701 42. C. Babiloni *et al.*, International Federation of Clinical Neurophysiology (IFCN)–EEG research
702   workgroup: Recommendations on frequency and topographic analysis of resting state EEG
703   rhythms. Part 1: Applications in clinical research studies. *Clinical Neurophysiology*, (2019).
704 43. R. C. Oldfield, The assessment and analysis of handedness: the Edinburgh inventory.
705   *Neuropsychologia* **9**, 97-113 (1971).
706 44. G. A. Taberna, R. Guarnieri, D. Mantini, SPOT3D: Spatial positioning toolbox for head markers
707   using 3D scans. *Scientific reports* **9**, 1-9 (2019).
708 45. Q. Liu *et al.*, Estimating a neutral reference for electroencephalographic recordings: the importance
709   of using a high-density montage and a realistic head model. *Journal of neural engineering* **12**,
710   056012 (2015).
711 46. R. D. Pascual-Marqui *et al.*, Assessing interactions in the brain with exact low-resolution
712   electromagnetic tomography. *Philos Trans A Math Phys Eng Sci* **369**, 3768-3784 (2011).
713 47. J. M. Lilly, S. C. Olhede, Generalized Morse Wavelets as a Superfamily of Analytic Wavelets. *Ieee
714   T Signal Proces* **60**, 6036-6041 (2012).
715 48. C. W. Fox, S. J. Roberts, A tutorial on variational Bayesian inference. *Artificial intelligence review*
716   **38**, 85-95 (2012).
717 49. M. Rubinov, O. Sporns, Complex network measures of brain connectivity: Uses and interpretations.
718   *Neuroimage* **52**, 1059-1069 (2010).

Author contribution

R.I., M.C. conceived the study. R.I., M.S. collected the data. R.I., M.S, D.S., S.B. and M.C. designed the methods. R.I., M.S. performed the analysis. R.I., M.S., D.M., L.A. and M.C. interpreted and discussed the results. R.I., M.C. prepared the figures. R.I. wrote the first version of the manuscript. All the authors contributed to the revision of the manuscript.

Competing Interest

All the authors declare no financial interest.

Data Availability

All data needed to evaluate the conclusions in the paper are present in the paper and/or the Supplementary Materials. Additional data related to this paper may be requested from the authors.
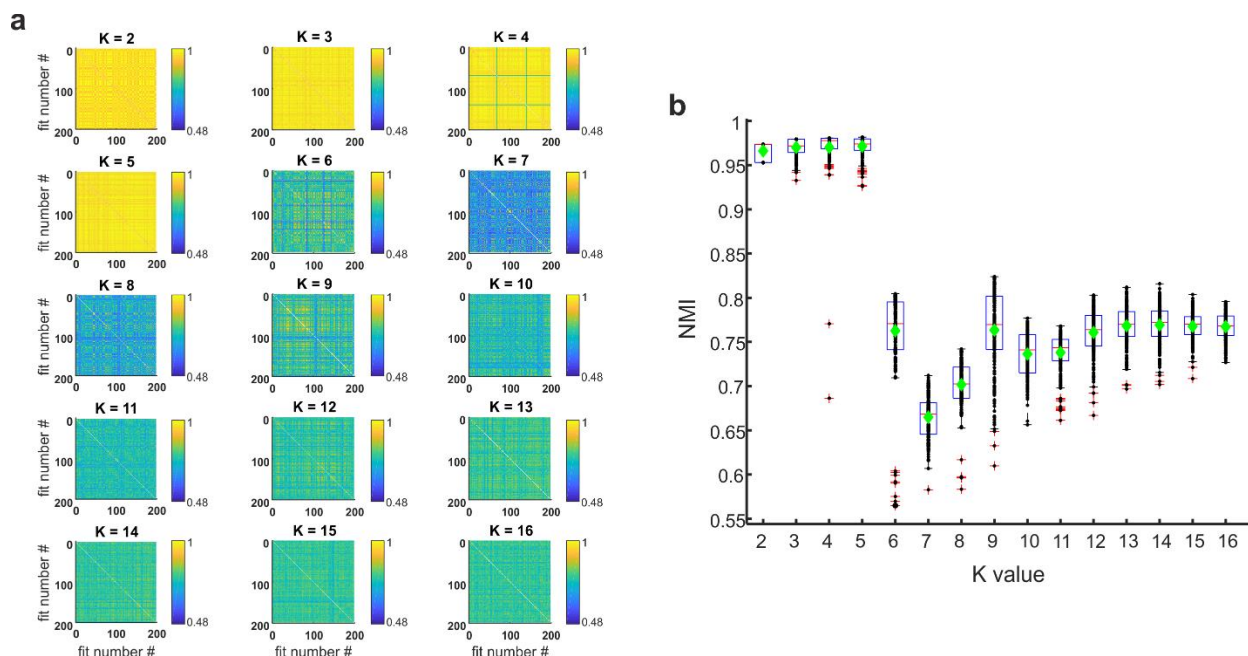
740 # **Supplementary Materials**

741 **Figure S1**

742

743 **Parameter selection conducted by means of Normalized Mutual Information (NMI)**. **a** Pairwise
744 comparisons of all the 200 fits from K = 2 until K = 16. Yellow and dark blue elements indicate respectively
745 a pair of fits showing a good (high NMI) and weak (low NMI) clustering performance, as indicated by the
746 color-bar. Self-fit comparisons are depicted in white. Note that all the matrices are symmetric. **b**
747 Distributions of the NMI values obtained by averaging the matrices containing the fits' pairwise
748 comparisons depicted in panel a. Boxplots' upper and lower boundary exhibited 25th and 75th percentile,
749 respectively. Data points (black dots) are overlaid over boxplots. Green diamonds and red lines indicates
750 mean and median value of the distributions, respectively. Red crosses indicate outliers. i.e. those fits for
751 which the WSBM algorithm found a solution that is far from almost all the remaining fits. The clustering
752 performance is reliable until K = 5 ("good performance", NMI values are close to one), unreliable otherwise
753 K ≥ 6 ("bad performance").

754

755

756

23

757   **Figure S2**
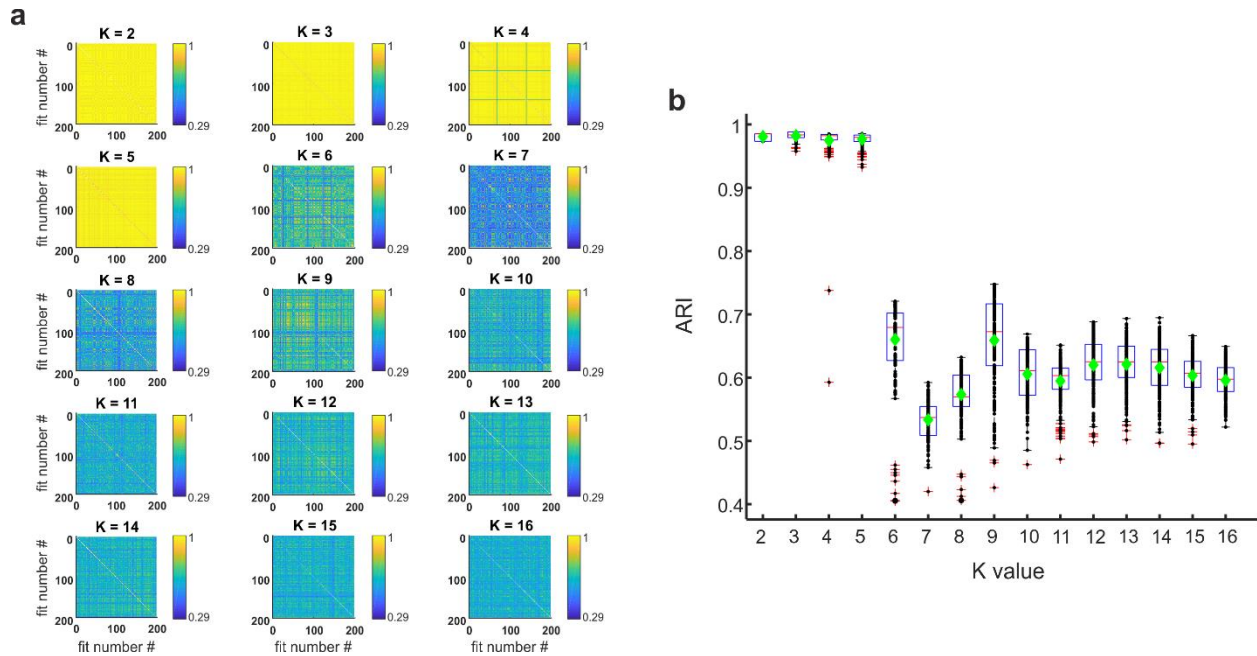

758

759   **Parameter selection conducted by means of Adjusted Rand Index (ARI). a** Pairwise comparisons of all
760   the 200 fits from K = 2 until K = 16. Yellow and dark blue elements indicate respectively a pair of fits
761   showing a good (high ARI) and weak (low ARI) clustering performance, as indicated by the color-bar. Self-
762   fit comparisons are depicted in white. Note that all the matrices are symmetric. **b** Distributions of the ARI
763   values obtained by averaging the matrices containing the fits' pairwise comparisons depicted in a. Boxplots'
764   upper and lower boundary exhibited 25th and 75th percentile, respectively. Data points (black dots) are
765   overlaid over boxplots. Green diamonds and red lines indicate the mean and median value of the
766   distributions, respectively. Red crosses are outliers i.e. those fits for which the WSBM algorithm found a
767   solution that is far from almost all the remaining fits. The clustering performance is reliable until K = 5
768   ("good performance", ARI values are close to one), unreliable otherwise K ≥ 6 ("bad performance").
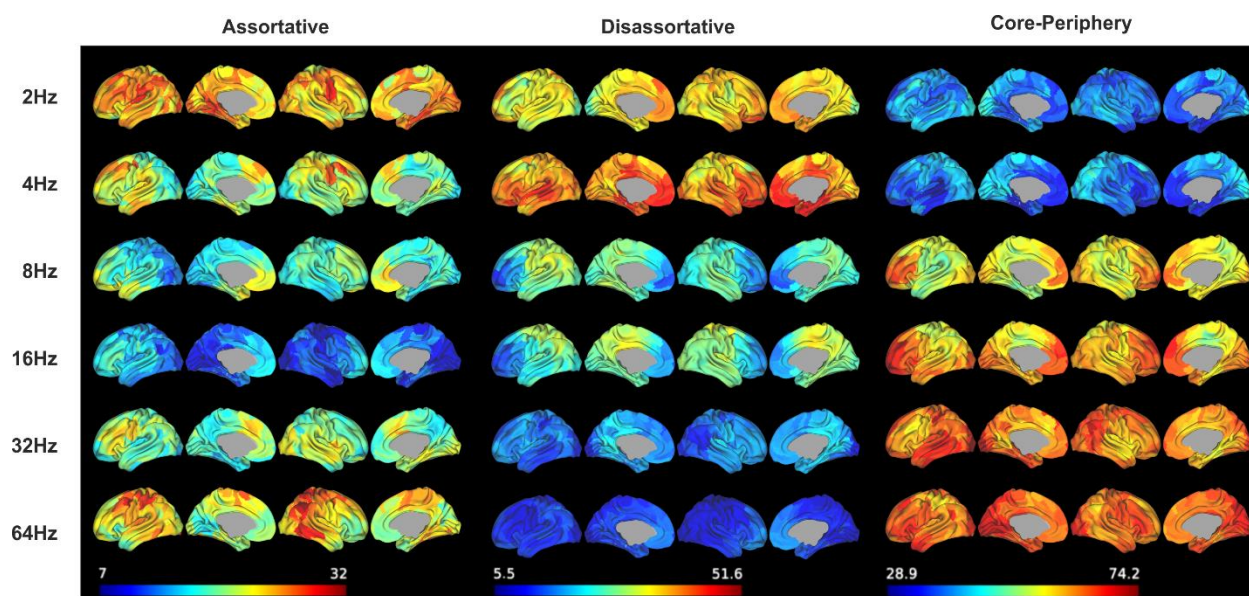
769

770   **Figure S3**
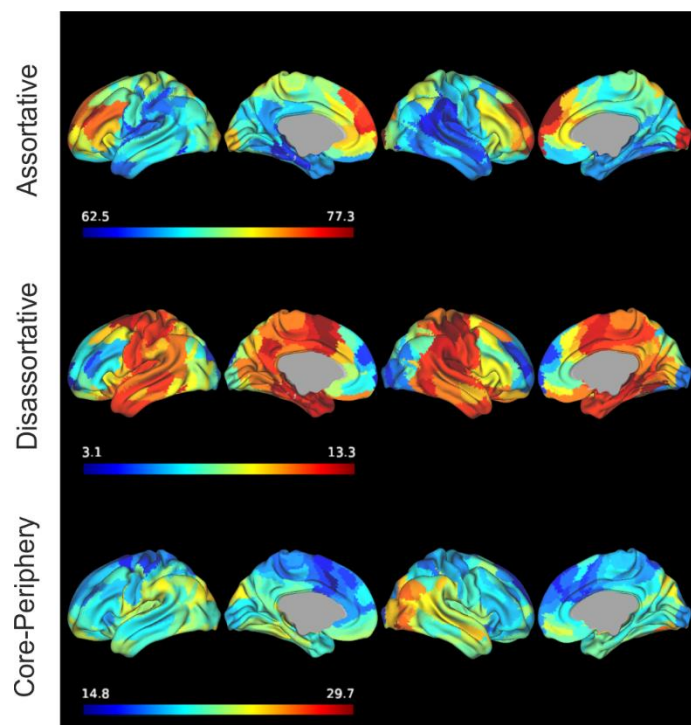
771

772   **Mean community interactions in the time domain across participants.** The color-bar is different for
773   each meso-scale modality to better appreciate region-specific variations. See Figure 3 in the main text where
774   the same plot is shown with a unique color-bar for all the interactions.

775

776 **Figure S4**

777

778 **Mean community interactions in the frequency domain across participants.** Each column indicates the
779 meso-scale class (assortative, disassortative, core-periphery) while each row indicates the carrier frequency
780 (2 Hz, 4 Hz, 8 Hz, 16 Hz, 32 Hz, 64 Hz). The color-bar is customized between minimum and maximum
781 values within each meso-scale modality. See Figure 6 in the main text where the same plot is showed with
782 a unique color-bar for all the interactions.

783

784

Table 1

Carrier	2 Hz	4Hz	8Hz	16 Hz	32 Hz	64 Hz
2 Hz		N.S.	N.S.	N.S.	0.006976	0.000052
4 Hz			N.S.	N.S.	0.000109	0.000000
8 Hz				N.S.	N.S.	N.S.
16 Hz					N.S.	0.045109
32 Hz						N.S.
64 Hz						

Non-parametric Kruskal-Wallis test for multiple comparisons across frequencies for the disassortative class.

Table 2

Carrier	2 Hz	4Hz	8Hz	16 Hz	32 Hz	64 Hz
2 Hz		N.S.	0.042072	0.002715	0.000630	0.001264
4 Hz			N.S.	0.005335	0.001312	0.002561
8 Hz				N.S.	N.S.	N.S.
16 Hz					N.S.	N.S.
32 Hz						N.S.
64 Hz						

Non-parametric Kruskal-Wallis test for multiple comparisons across frequencies for the core-periphery class.

Note that assortative interactions across frequencies were non-statistically significant and thus we did not perform the multiple comparison test.

798 **T1-weighted structural images acquisition**

799 Subjects underwent T1-weighted using either a 3T or 1.5 T scanners. See Supplementary Table 3 for the
800 T1-weighted acquisition parameters.

801 **Table 3**

Number of subject	21	7	4
MRI scanner	3T Achieva (Philips Medical System, The Netherlands)	3 T MAGNETOM Prisma (Siemens AG, Healthcare Sector, Germany)	1.5 T Signa Excite (General Electric Healthcare, USA)
T1-weighted sequence name	Magnetization Prepared Rapid Acquisition Gradient Echo (MPRAGE)	Magnetization Prepared Rapid Acquisition Gradient Echo (MPRAGE)	Fast Spoiled Gradient Echo (SPGR)
Coil	32-channel head coil	32-channel head coil	8-channels phased array head coil
Voxel Size	$0.98{\times}0.98{\times}1.2$ mm^3	$1{\times}1{\times}1$ mm^3	$1{\times}1{\times}1$ mm^3
TR/TE	9.6/4.6 ms	2.3/2.96 ms	11.8/5.18 ms
Field of View (F.O.V)	250x250 mm^2	$256{\times}256$ mm^2	$256{\times}256$ mm^2

802